

**Measurement of jets produced in top quark events using the  $e\mu$  final state with  
2  $b$ -tagged jets in  $pp$  collisions at  $\sqrt{s} = 8$  TeV with the ATLAS detector**

by

Jacquelyn Kay Brosamer

A dissertation submitted in partial satisfaction of the

requirements for the degree of

Doctor of Philosophy

in

Physics

in the

Graduate Division

of the

University of California, Berkeley

Committee in charge:

Professor Marjorie Shapiro, Chair

Professor Leo Blitz

Professor Barbara Jacak

Fall 2015

The dissertation of Jacquelyn Kay Brosamer, titled Measurement of jets produced in top quark events using the  $e\mu$  final state with 2  $b$ -tagged jets in  $pp$  collisions at  $\sqrt{s} = 8$  TeV with the ATLAS detector, is approved:

Chair	_____	Date	_____
	_____	Date	_____
	_____	Date	_____

University of California, Berkeley

**Measurement of jets produced in top quark events using the  $e\mu$  final state with  
2  $b$ -tagged jets in  $pp$  collisions at  $\sqrt{s} = 8$  TeV with the ATLAS detector**

Copyright 2015  
by  
Jacquelyn Kay Brosamer

## Abstract

Measurement of jets produced in top quark events using the  $e\mu$  final state with 2  $b$ -tagged jets in  $pp$  collisions at  $\sqrt{s} = 8$  TeV with the ATLAS detector

by

Jacquelyn Kay Brosamer

Doctor of Philosophy in Physics

University of California, Berkeley

Professor Marjorie Shapiro, Chair

The transverse momentum ( $p_T$ ) and multiplicity of jets produced in top quark events are measured using  $20.3 \text{ fb}^{-1}$  of  $pp$  collision data at a center-of-mass energy of  $\sqrt{s} = 8$  TeV. Jets are selected from top events requiring an opposite-charge  $e\mu$  pair and two  $b$ -tagged jets in the final state. The data are corrected to obtain the particle-level fiducial cross section  $\frac{1}{\sigma_{e\mu+2 \text{ } b\text{-jets}}} \frac{d\sigma_{\text{jet}}}{dp_T}$  for additional jets with rank 1-4, where rank=1 is the leading additional jet. These distributions are used to obtain the extra jet multiplicity as a function of minimum jet  $p_T$  threshold.

# Contents

<b>Contents</b>	<b>i</b>
<b>List of Figures</b>	<b>iv</b>
<b>List of Tables</b>	<b>vi</b>
<b>1 Introduction</b>	<b>1</b>
<b>2 Theory</b>	<b>2</b>
2.1 The Standard Model . . . . .	2
2.1.1 Particles of the SM . . . . .	2
2.1.2 Electroweak theory . . . . .	3
2.1.3 Quantum chromodynamics . . . . .	3
2.1.3.1 Factorization . . . . .	4
2.1.4 Beyond the SM . . . . .	5
2.2 Top quark physics . . . . .	6
2.2.1 Top quark production at the LHC . . . . .	7
2.2.2 Top quark decays . . . . .	7
2.3 QCD in hadron-hadron collisions . . . . .	8
<b>3 Analysis strategy</b>	<b>15</b>
3.1 Event selection . . . . .	15
3.2 Extra jets . . . . .	15
3.3 Correction procedure . . . . .	15
3.4 Evaluation of generators . . . . .	15
<b>4 The ATLAS detector and the LHC</b>	<b>16</b>
4.1 The Large Hadron Collider . . . . .	16
4.1.1 Accelerator Complex . . . . .	17
4.1.2 Beam conditions . . . . .	18
4.2 Overview of the ATLAS detector . . . . .	20
4.3 Inner detector . . . . .	20
4.3.1 Pixel detector . . . . .	20

4.3.2	SemiConductor Tracker . . . . .	20
4.3.3	Transition Radiation Tracker . . . . .	20
4.3.4	Track reconstruction . . . . .	20
4.4	Calorimeters . . . . .	20
4.4.1	Electromagnetic calorimeter . . . . .	20
4.4.2	Hadronic calorimeter . . . . .	20
4.5	Muon spectrometer . . . . .	20
4.6	The trigger system . . . . .	20
4.6.1	Electron trigger . . . . .	20
4.6.2	Muon trigger . . . . .	20
<b>5</b>	<b>Event reconstruction and object definitions</b>	<b>22</b>
5.1	Object reconstruction and selection . . . . .	22
5.1.1	Charged tracks . . . . .	22
5.1.2	Primary vertex . . . . .	22
5.1.3	Electron . . . . .	22
5.1.4	Muon . . . . .	22
5.1.5	Jets . . . . .	22
5.1.6	$b$ -jet identification . . . . .	22
5.2	Particle-level definitions . . . . .	22
<b>6</b>	<b>Event selection</b>	<b>23</b>
6.1	Data samples . . . . .	23
6.1.1	Collision data . . . . .	23
6.1.2	Monte Carlo samples . . . . .	23
6.1.2.1	$t\bar{t}$ . . . . .	23
6.1.2.2	Single top $Wt$ . . . . .	23
6.1.2.3	Other physics processes . . . . .	23
6.2	Event selection . . . . .	23
6.2.1	Event yields . . . . .	23
6.2.2	Reconstructed distributions . . . . .	23
<b>7</b>	<b>Reconstruction of extra jets</b>	<b>24</b>
7.1	Matching criteria . . . . .	24
7.2	Background contributions . . . . .	24
7.3	Reconstruction level distributions . . . . .	24
<b>8</b>	<b>Correction to particle-level</b>	<b>25</b>
8.1	Introduction to unfolding . . . . .	25
8.2	Procedure . . . . .	25
8.2.1	Binning . . . . .	25
8.2.2	Bias in extra jets from event selection requirements . . . . .	25

8.2.2.1	Study of biases . . . . .	25
8.2.2.2	Correction factor . . . . .	25
8.3	Validation . . . . .	25
8.3.1	Closure test . . . . .	25
8.3.2	Stress test . . . . .	25
8.4	$\chi^2$ evaluation . . . . .	25
<b>9</b>	<b>Sources of uncertainty</b>	<b>26</b>
9.1	Types of uncertainty . . . . .	26
9.2	Detector modeling . . . . .	26
9.3	Single top rate . . . . .	26
9.4	Background extra jets . . . . .	26
9.5	Input extra jet spectrum . . . . .	26
9.6	Combined uncertainty . . . . .	26
<b>10</b>	<b>Results</b>	<b>27</b>
10.1	Fully corrected distributions . . . . .	27
10.2	$\chi^2$ comparisons . . . . .	27
10.3	Discussion . . . . .	27
<b>11</b>	<b>Conclusions</b>	<b>28</b>
<b>A</b>	<b>Extra jets</b>	<b>29</b>
<b>B</b>	<b>Tracking studies</b>	<b>30</b>
<b>C</b>	<b>Modeling hadron decays</b>	<b>31</b>
	<b>Bibliography</b>	<b>32</b>

# List of Figures

2.1	Summary of measurements of $\alpha_S$ as a function of the respective energy scale, $Q$ , from Ref. [17]. The respective degree of QCD perturbation theory used in the extraction of $\alpha_S$ is indicated in brackets (NLO: next-to-leading order; NNLO: next-to-next-to leading order; res. NNLO: NNLO matched with resummed next-to-leading logs; N3LO: next-to-NNLO). . . . .	10
2.2	Diagram from Ref. [?] illustrating the structure of a generic hard scattering process of two incoming partons $A$ and $B$ with PDFs $f_{a/A}$ and $f_{b/B}$ . . . . .	11
2.3	Summary of the ATLAS direct $m_{top}$ measurements. The results are compared with the ATLAS, Tevatron and Tevatron+LHC $m_{top}$ combinations. For each measurement, the statistical uncertainty, the sum of the remaining uncertainties are reported separately. The JSF, bJSF contributions are statistical in nature and apply to analyses performing in-situ (top quark pair base) jet energy calibration procedures. . . . .	12
2.4	Feynman diagrams for $t\bar{t}$ production at leading order QCD . . . . .	12
2.5	Summary of LHC and Tevatron measurements of the top-pair production cross-section as a function of the centre-of-mass energy compared to the NNLO QCD calculation complemented with NNLL resummation (top++2.0). The theory band represents uncertainties due to renormalisation and factorisation scale, parton density functions and the strong coupling. The measurements and the theory calculation is quoted at $m_{top}=172.5$ GeV. Measurements made at the same centre-of-mass energy are slightly offset for clarity. . . . .	13
2.6	Summary of ATLAS measurements of the single top production cross-sections in various channels as a function of the center of mass energy compared to a theoretical calculation based on NLO QCD complemented with NNLL resummation. For the $s$ -channel only an upper limit is shown. . . . .	14
2.7	Feynman diagrams for single top quark production at leading order QCD. From left to right: $t$ -channel production as flavor excitation; $t$ -channel production as $W$ -gluon fusion; $s$ -channel production; $Wt$ -channel production. . . . .	14
4.1	The location of the four main LHC experiments: ALICE, ATLAS, CMS and LHCb. The LHC tunnel is 27 km in circumference, situated underneath the border of France and Switzerland, near the city of Geneva, as shown. [6]. . . . .	17



4.2	The LHC accelerator complex boosts particles to increasingly higher energies before reaching the LHC. The particle beams are accelerated successively by Linac 2, the Proton Synchrotron Booster (PSB), the Proton Synchrotron (PS), the Super Proton Synchrotron (SPS) and then finally enter the LHC rings [14]. .	18
4.3	Cumulative luminosity versus time delivered to (green), recorded by ATLAS (yellow), and certified to be good quality data (blue) during stable beams and for pp collisions at 8 TeV centre-of-mass energy in 2012. Luminosity can be lost due to data acquisition inefficiency or other effects. . . . .	20
4.4	Luminosity-weight distribution of the mean number of interactions per bunch crossing. Both the full data from the 2011 and 2012 <i>pp</i> runs at the LHC are shown.	21

# List of Tables

2.1	Spin and charge of particles in the SM. . . . .	9
2.2	Mass of particles in the SM, taken from Ref. [17]. . . . .	9

## Acknowledgments

To do

# Chapter 1

## Introduction

# Chapter 2

## Theory

This chapter reviews some of the theoretical concepts relevant to the subsequent physics analysis. The importance of the top quark within the Standard Model is first discussed. The modeling of physics at hadron colliders is also reviewed.

### 2.1 The Standard Model

The SM of particle physics is one of the most precisely tested and successful theories in the history of physics [18]. The theory represents the best current understanding of the fundamental behavior of subatomic particles and provides the framework for particle physics predictions. All predictions of the SM have been verified and found to be self-consistent up to the Planck scale ( $10^{15-19}$  GeV).

The SM uses the mathematical framework of Quantum Field Theory (QFT) to describe two kinds of particles, fermions and bosons. Fundamental interactions between these particles can be derived from the conservation of a symmetry called gauge invariance. This general principle maps all conserved quantities to the invariance of the Lagrangian under some transformation, an aesthetically appealing idea known as Noether's theorem. The SM provides a unified description of the strong, weak and electromagnetic forces, but does not (yet) include gravity. The symmetry group of the SM is  $SU(3) \times SU(2) \times U(1)$ .

#### 2.1.1 Particles of the SM

Tables ??-?? summarize the properties of the fundamental particles of the SM described below.

Fermions are spin- $\frac{1}{2}$  point-like particles that form ordinary matter. The two types of fermions are known as leptons and quarks. The three lepton generations, each with a charged lepton and a neutrino, interact via the electroweak force. The three quark generations, each with an up-type and down-type quark, interact via both the electroweak force and the strong force. The strong force combines quarks into composite particles. Three such quarks form a

baryon, while two quarks form a meson. Each fermionic generation is identical to the first, except for mass.

Bosons are particles with integer spin that mediate interactions between particles. Each gauge boson corresponds to a different fundamental force, and the range each force is inversely related to the boson mass.

**Electromagnetic (EM) force** mediated by the massless and chargeless photon ( $\gamma$ ). Since the photon is massless, the range of the EM force is infinite. The EM force is responsible for many common interactions, such as radiation of photons from excited atoms.

**Weak force** mediated by the  $W^\pm$  and  $Z^0$  bosons and is responsible for nuclear reactions such as beta decay .

**Strong force** mediated by gluons ( $g$ ) is responsible for the formation of protons and neutrons. The quarks are the only fermions that interact strongly.

Discovered in 2012, the Higgs boson is the final particle in the SM. In order to explain the mass difference between the photon and electroweak bosons, the symmetry between the EM and weak forces must be broken. The Higgs field interacts with the electroweak gauge bosons to provide masses while preserving the local gauge invariance of the SM.

### 2.1.2 Electroweak theory

At low energy, the EM and weak forces appear distinct. Above the unification energy ( $\sim 100\text{GeV}$ ), the EM and weak forces are unified into a single interaction known as the electroweak interaction. The corresponding symmetry group is  $SU(2) \times U(1)$ , where  $SU(2)$  represents the weak force and  $U(1)$  represents the EM force. MORE FROM PDG

### 2.1.3 Quantum chromodynamics

Quantum chromodynamics (QCD) is a gauge theory which interactions between quarks via the strong force. The six flavors of quarks ( $u, d, s, c, b$  and  $t$ ) each carry a conserved quantum number called color, which is analogous to electric charge in QED. Neither quarks nor gluons can exist as free particles. Instead, color-neutral combinations of quarks, anti-quarks and gluons called hadrons are observed.

The QCD Lagrangian for the interaction between two quarks  $i$  and  $j$  can be written as [17]:

$$\mathcal{L}_{QCD} = \bar{\psi}_i(i\gamma^\mu\partial_\mu\delta_{ij} - g_s\gamma^\mu t_{ij}^C\mathcal{A}_\mu^C - m\delta_{ij})\psi_j - \frac{1}{4}G_{\mu\nu}^A G_A^{\mu\nu}, \quad (2.1)$$

$$\text{where } G_{\mu\nu}^A \equiv \partial_\mu\mathcal{A}_\nu^A - \partial_\nu\mathcal{A}_\mu^A - g_s f_{ABC}\mathcal{A}_\mu^B\mathcal{A}_\nu^C, \quad (2.2)$$

where repeated indices are summed over,  $\gamma^\mu$  are the Dirac  $\gamma$  matrices.  $\psi_i$  is the quark-field spinor, where the color index  $i$  can correspond to one of three ( $N_C$ ) quark flavors.  $\mathcal{A}_\mu^B$

represents the gluon fields, where  $C$  runs from 1 to  $N_C^2 - 1 = 8$ , corresponding to eight types of gluons.  $t^A$  are the eight  $3 \times 3$  generating matrices of  $SU(3)$  and  $f_{ABC}$  the group structure constants of  $SU(3)$ . The fundamental parameters are the coupling  $g_s$  and the quark masses  $m$ .

The structure of the Lagrangian predicts three types of vertices: a quark-antiquark-gluon ( $q\bar{q}g$ ) vertex proportional to  $g_s$ , a three gluon vertex proportional to  $g_s$ , and a four gluon vertex proportional to  $g_s^2$ . Since gluons carry color charge, they can directly couple to other gluons, unlike other bosons. These self-interaction vertices mean that QCD has divergent terms that are not found in other SM sectors.

Perturbative QCD calculations at next-to-leading order and beyond necessarily involve these divergent quark and gluon loops. These divergences must be removed in order to obtain a physical result. In order to remove the divergences, the strong coupling constant must be “renormalized” and expressed as a function of an (unphysical) renormalization scale  $\mu_R$ . Notably, QCD predictions change depending on the scale of the probe. This is sometimes referred to as the “running” of the coupling constant. Predictions for a given process are evaluated with  $\mu_R$  as close to the momentum transfer  $Q$  as possible, so that  $\alpha_s(\mu_R \simeq Q)$  gives the effective strength of the strong force in that particular process.

The strong coupling constant  $\alpha_S \equiv g_s^2/4\pi$  is related the renormalization scale  $\mu_R$  by the renormalization group equation (RGE):

$$\mu_R^2 \frac{\alpha_S}{\mu_R^2} = \beta(\alpha_S) = - (b_0 \alpha_S^2 + b_1 \alpha_S^3 + b_2 \alpha_S^4 + \dots) \quad (2.3)$$

where the coefficients  $b$  are called the beta-function coefficients and depend on the number of quark colors. The values of the beta coefficients up to  $b_3$  can be found in Ref. [?].

Figure 2.1 shows the next-to-leading-order QCD prediction for  $\alpha_S$  as a function of  $Q$ , as well as several experimentally measured values of  $\alpha_S$  for discrete energy scales. Experimental measurement agrees very well with the theoretical predictions. The negative sign on the right side of Eqn.2.3 means that the strong coupling becomes weaker as the scale increases:  $\alpha_S \sim 0.1$  for momentum transfers  $100 \text{ GeV} \lesssim Q \lesssim 1 \text{ TeV}$ . This is the origin of the previously mentioned asymptotic freedom, which allows partons to be considered approximately free at high energy. The divergence of the coupling constant at low energy results in the formation of stable hadrons and is called “confinement.”

### 2.1.3.1 Factorization

Because of the scale dependence of QCD, interactions can be separated into two regimes, with the transition around the QCD confinement scale,  $\Lambda_{QCD} \sim 200 \text{ MeV}$ , the energy at which QCD became non-perturbative. At low energy,  $\alpha_S$  is of order unity, so perturbative expansion is not possible. The quarks are bound together by soft gluon emissions into a proton. At scales far above the QCD confinement scale, the partons can be considered free objects and can be treated with perturbative expansion.

The hard scatter interaction with momentum transfer  $Q$  occurs on a time scale that goes as  $\tau \sim 1/Q$  which is much larger than the time scale of interactions between protons  $\tau \sim 1/\Lambda_{QCD}$ . This fact allows high energy proton collisions to be *factorized* into two independent processes: the Parton Distribution Function (PDF), which is a phenomenological description of the momentum distribution among the partons inside the proton which depends only on the momentum scale, and the partonic cross section  $\hat{\sigma}$ , which uses perturbative QCD to determine the calculation of the scatter of the hard probe from one of the free partons inside the proton.

Specifically, the hadronic cross-section for a particular process can be written the weighting of the subprocess cross section with the PDFs  $f_{q/A}(x)$  extracted from deep inelastic scattering experiments[?]:

$$\begin{aligned}\sigma(AB \rightarrow X) &= \int dx_a dx_b f_{a/A}(x_a, \mu_F^2) f_{b/B}(x_b, \mu_F^2) \hat{\sigma}_{ab \rightarrow X} \\ &= \int dx_a dx_b f_{a/A}(x_a, \mu_F^2) f_{b/B}(x_b, \mu_F^2) \times [\sigma_0 + \alpha_S(\mu_R^2) \sigma_1 + \dots] \quad (2.4)\end{aligned}$$

which is diagrammatically represented in Figure 2.2. The partonic cross-section can be perturbatively expanded in powers of the strong coupling constant  $\alpha_S$  for some renormalization scale  $\mu_R$ . The PDF  $f_{a/A}(x_a, \mu_F^2)$  gives the probability that a proton with momentum  $p_A$  contains a parton  $a$  with momentum  $p_a$ . This function depends only on the fraction of the proton momentum distributed to parton  $a$ ,  $x_a \equiv p_a/p_A$ , and the factorization scale  $\mu_F$ .

Since the PDF part of the cross section is in the non-perturbative regime of QCD, PDFs must be determined by global fits to experimental measurements of deep inelastic and other hard-scattering processes. PDFs derived from measurements of one process can be used for predictions in a different process. For example, positron-proton scattering data from the HERA experiment can be used to make predictions for proton-proton collision at the LHC.

PDF measurements depend on the scale of the hard probe, so theoretical calculations are needed to evolve the PDFs between experimental data points. The differential equations governing the  $\mu^2$  dependence of the PDFs are called the DGLAP equations and are derived in Ref. [?]. Much like the RGE introduces an arbitrary  $\mu_R$ , the DGLAP equations introduce a factorization scale  $\mu_F$  to absorb the divergences from soft parton emissions. To avoid unnaturally large logarithms in the perturbative expansion,  $\mu_F$  and  $\mu_R$  are usually assumed to be equal and of the order of the typical momentum scales of the hard scattering process. The theoretical uncertainty from the arbitrary choice of  $\mu_F$  and  $\mu_R$  is usually evaluated by repeating the calculation with the scale doubled and halved.

### 2.1.4 Beyond the SM

In addition to providing a test of the SM, the top quark may also provide a window to physics at higher energy scales beyond the SM.

The top quark is important in aesthetic problem with the Higgs mass known as the hierarchy problem or fine tuning. The Higgs mechanism provides an explanation for elec-



electroweak symmetry breaking and acquisition of mass by other SM particles. As a scalar particle, the Higgs receives higher-order corrections to its physical (measured) mass from interactions with fermions, gauge bosons and itself. These corrections are on the order of the Planck scale,  $\mathcal{O}(\Lambda^2 \approx 10^{30-38} \text{ GeV})$ , while the observed mass is close to the electroweak scale,  $\mathcal{O}(100 \text{ MeV})$ . Thus, in order to obtain the observed mass without introducing new physics, there must be an unnatural canceling. Since the dominant higher-order correction to the Higgs mass comes from the top, precisely measuring the top's mass and other properties may provide insight to this problem.

In addition to the hierarchy problem, there are several other open questions which cannot be explained by the SM. The SM does not account for the 85% of our universe made up of *dark matter* particles, or provide an explanation for the observed asymmetry between matter and anti-matter. The SM also does not account for the observed non-zero mass of neutrinos or have a way to incorporate gravitational interactions.

Theorists have formulated many extensions to the SM that address these puzzles. Perhaps the most widespread, Supersymmetry (SUSY) [16] proposes an additional superpartner for every particle in the SM. SUSY is especially popular because it naturally contains a light, stable, neutral dark matter candidate and solves the hierarchy problem. Diagrams from superpartners remove the need to fine tune the Higgs mass. Since SUSY has not been observed, the superpartners of SM particles must have different masses, and SUSY has to be a broken symmetry. However, in order to satisfactorily solve the hierarchy problem, the superpartners with the largest contributions to the Higgs mass must be  $\mathcal{O}(\text{TeV})$ . This means that they should be discoverable at the LHC.

Another popular SM extension, called the Randall-Sundrum model [15], posits an extra dimension in which gravity would propagate. This model includes a new particle, a Kaluza-Klein gluon, that propagates into the extra dimension and decays into a top quark pair.

Many of the signals for new physics are dominated by the top quark since heavier particles are more sensitive to higher energy scales. The top pair production analyzed in this thesis is important as a background for  $t\bar{t}$  resonances [5] and other searches [8].

## 2.2 Top quark physics

The top quark was first discovered at Fermilab in 1995 [10][9]. As the heaviest known fundamental particle, the top quark is an important probe of the Standard Model (SM) and extensions of the SM. Before the Large Hadron Collider (LHC), the Tevatron provided the only experimental observation of the top. The LHC produces a top quark every few seconds, about a hundred times more frequently than the Tevatron. This significant increase in statistics allows precision measurements of the top at the LHC, which is sometimes called a "Top Factory."

Because of its large mass, the top quark plays a special role in the SM. The top mass is about the same as a gold atom nucleus, 40 times larger than the next heaviest quark and  $10^5$  times heavier than the lightest quark. The mass of the top quark has been precisely

measured in different decay channels at both the LHC and the Tevatron. Figure 2.3 shows a recent summary of these measurements, which can be combined to give a world average of  $173.34 \pm 0.76$  for the top quark mass.

The top has a very short lifetime ( $\sim 5 \times 10^{-25}$  s), so it is the only quark that decays before it can form a hadron with other quarks. This unique property means that the top is the only “bare” quark that can be accessed at the LHC. The top is also the only quark with Yukawa coupling to the Higgs boson of order unity. Thus, accurately measuring its properties (mass, coupling, cross section, branching ratios) provides an important information about Quantum Chromodynamics (QCD), the SM description of interactions between quarks via the strong force.

### 2.2.1 Top quark production at the LHC

In  $pp$  collision at the LHC, top quarks are mostly produced in pairs through the leading order QCD processes  $gg \rightarrow t\bar{t}$  and  $q\bar{q} \rightarrow t\bar{t}$ . The Feynman diagrams for these processes are shown in Figure 2.4. At Tevatron with  $p\bar{p}$  collisions,  $t\bar{t}$  production was dominated by quark annihilation ( $\sim 85\%$ ). At the LHC, the higher collision energy and lack of valence anti-quarks in the proton result in gluon-fusion dominated  $t\bar{t}$  production ( $\sim 85\%$ ) [17]. The total  $t\bar{t}$  cross-section has been computed at next-to-next-to leading order (NNLO) with next-to-next-to-leading-log soft gluon resummation (NNLL) in Ref. [12] with a final theoretical uncertainty of  $\sim 3\%$  and found to agree with experimental measurements. Figure 2.5 compares this calculation with measurements made at both in the LHC and Tevatron in various decay channels.

Top quarks can also be produced singly via electroweak processes. Because the weak coupling is much smaller than the strong coupling, fewer quarks are produced singly than in pairs. The Feynman diagrams for single top production are shown in Figure 2.7. Single production can be mediated by virtual  $s$ -channel and  $t$ -channel  $W$ -bosons. These production channels provide sensitivity to physics beyond the SM. Single tops are also produced in association with a  $W$ -boson ( $Wt$ -associated production). While negligible at the Tevatron, at the LHC,  $Wt$ -associated production provides a sizeable contribution to single top production. The inclusive cross-section for  $s$ -channel,  $t$ -channel and  $Wt$ -associated single top production has been computed to NNLO. This calculation is compared with the ATLAS experimental measurements of each channel in Figure 2.6.

### 2.2.2 Top quark decays

At lowest order in the SM, the top quark can only decay to a  $W$  boson and a down-type quark:  $t \rightarrow qW$  where  $q = b, s, d$ . The rate of each of these decays is proportional to the square of the Cabibbo-Kobayashi-Masakawa (CKM) matrix,  $|V_{tq}|^2$ . Measured from experiment, the CKM matrix governs quark mixing in flavor-changing weak decays [17].

Weak hadron decays and the unitarity of the CKM matrix constrain the value of  $0.9990 < |V_{tb}| < 0.9992$  at the 95% C.L. [?]. Top quarks nearly always decay with  $t \rightarrow Wb$ .

Experimentally, the decay modes of  $t\bar{t}$  are distinguished by the decay of the two  $W$ -bosons:

**All hadronic** Both  $W$  bosons decay to quark pairs:  $t\bar{t} \rightarrow WbWb \rightarrow bbqqqq$ . Because there are 6 quarks in the final state, this channel has a large multi-jet background, which can be difficult to subtract.

**Semi-leptonic** One  $W$  boson decays to a quark pair and the other decays to a lepton and neutrino:  $t\bar{t} \rightarrow WbWb \rightarrow bbqq\ell\nu$ . This channel can be further categorized by lepton flavor.

**Dileptonic** Both  $W$  bosons decay to leptons:  $t\bar{t} \rightarrow WbWb \rightarrow bb\ell\nu\ell\nu$ . Though the dilepton channel has the fewest events, it often provides least background.

## 2.3 QCD in hadron-hadron collisions

The protons collided at the LHC are composite objects made of point-like quarks held together by soft gluon emissions. Because of the asymptotic freedom of QCD,  $\alpha_S$  is of order unity at the scale of these emissions within the proton, but as the scale of emissions increase  $\alpha_S$  quickly drops. Then, at scales far above the QCD confinement scale ( $\Lambda_{QCD} \sim 200$  MeV, the energy at which QCD became non-perturbative), the protons can be considered free objects. The hard scatter interaction with momentum transfer  $Q$  occurs on a time scale that goes as  $\tau \sim 1/Q$  which is much larger than the time scale of interactions between protons  $\tau \sim 1/\Lambda_{QCD}$ . This fact allows high energy proton collisions to be *factorized* into two independent processes: the Parton Distribution Function (PDF), which describes the momentum distribution among the partons inside the proton and depends only on the momentum scale, and the partonic cross section  $\hat{\sigma}$ , which uses perturbative QCD to determine the calculates the scatter of the hard probe from one of the free partons inside the proton.

### PDF STUFF

Then, the final  $t\bar{t}$  cross section ( $\sigma_{t\bar{t}}$ ) is a convolution of the partonic cross section ( $q\bar{q}, qq \rightarrow t\bar{t}$ ) and the parton distribution functions (PDFs) [?]:

$$\sigma_{t\bar{t}}(s, m_t) = \sum_{i,j} \int_0^1 dx_i \int_0^1 dx_j f_i(x_i, \mu_F^2) f_j(x_j, \mu_F^2) \times \hat{\sigma}_{ij}(\hat{s}, m_t, \alpha_s(\mu_R), \mu_R) \quad (2.5)$$

### DISCUSSION OF GLUON GLUON ETC AT LHC

At the LHC,  $qg$  scattering occurs with the highest parton luminosity but the partonic cross-section  $\hat{\sigma}_{qg}$  is smaller than either  $\hat{\sigma}_{gg}$  or  $\hat{\sigma}_{qq}$ . The largest contribution for top pair production at the LHC comes from gluon-gluon fusion, due to the combination of a large partonic cross-section and the second largest parton luminosity. The second largest contribution comes from quark-antiquark annihilation. At NLO QCD, the total  $t\bar{t}$  production at the LHC comprises approximately 90%

	particles			spin	electric charge
Quarks	$(u, d)_L$	$(c, s)_L$	$(t, b)_L$	$(\frac{1}{2}, \frac{1}{2})$	$(+\frac{2}{3}, -\frac{1}{3})$
	$u_R$	$c_R$	$t_R$	$\frac{1}{2}$	$+\frac{2}{3}$
	$d_R$	$s_R$	$b_R$	$\frac{1}{2}$	$-\frac{1}{3}$
Leptons	$(\nu_e, e^-)_L$	$(\nu_\mu, \mu^-)_L$	$(\nu_\tau, \tau^-)_L$	$(\frac{1}{2}, \frac{1}{2})$	$(0, -1)$
	$e_R^-$	$\mu_R^-$	$\tau_R^-$	$\frac{1}{2}$	-1
Gauge bosons	$g$			1	0
	$W^\pm$ and $Z$			1	$\pm 1$ and 0
	$\gamma$			1	0
Scalar boson	$H$			0	0

Table 2.1: Spin and charge of particles in the SM.

	Particle	Mass
Leptons	$e$	0.511 MeV
	$\mu$	105 MeV
	$\tau$	1777 MeV
Gauge bosons	$W^\pm$	80.2 GeV
	$Z$	91.19 GeV
	$H$	126 GeV
Quarks	up ( $u$ )	1.7-3.3 MeV
	down ( $d$ )	4.1-5.8 MeV
	charm ( $c$ )	1.18-1.34 GeV
	strange ( $s$ )	70-120 MeV
	top ( $t$ )	$173.34 \pm 0.76$ GeV[7]
	bottom ( $b$ )	$4.18 \pm 0.03$ GeV
Hadrons	$p$	938 MeV
	$n$	939 MeV
	$\pi^\pm$	139.6 MeV
	$\pi^0$	135.0 MeV

Table 2.2: Mass of particles in the SM, taken from Ref. [17].

At the Tevatron, a previous  $p\bar{p}$  collider with lower energy,  $t\bar{t}$  production was  
 AHHH REPETITIVE

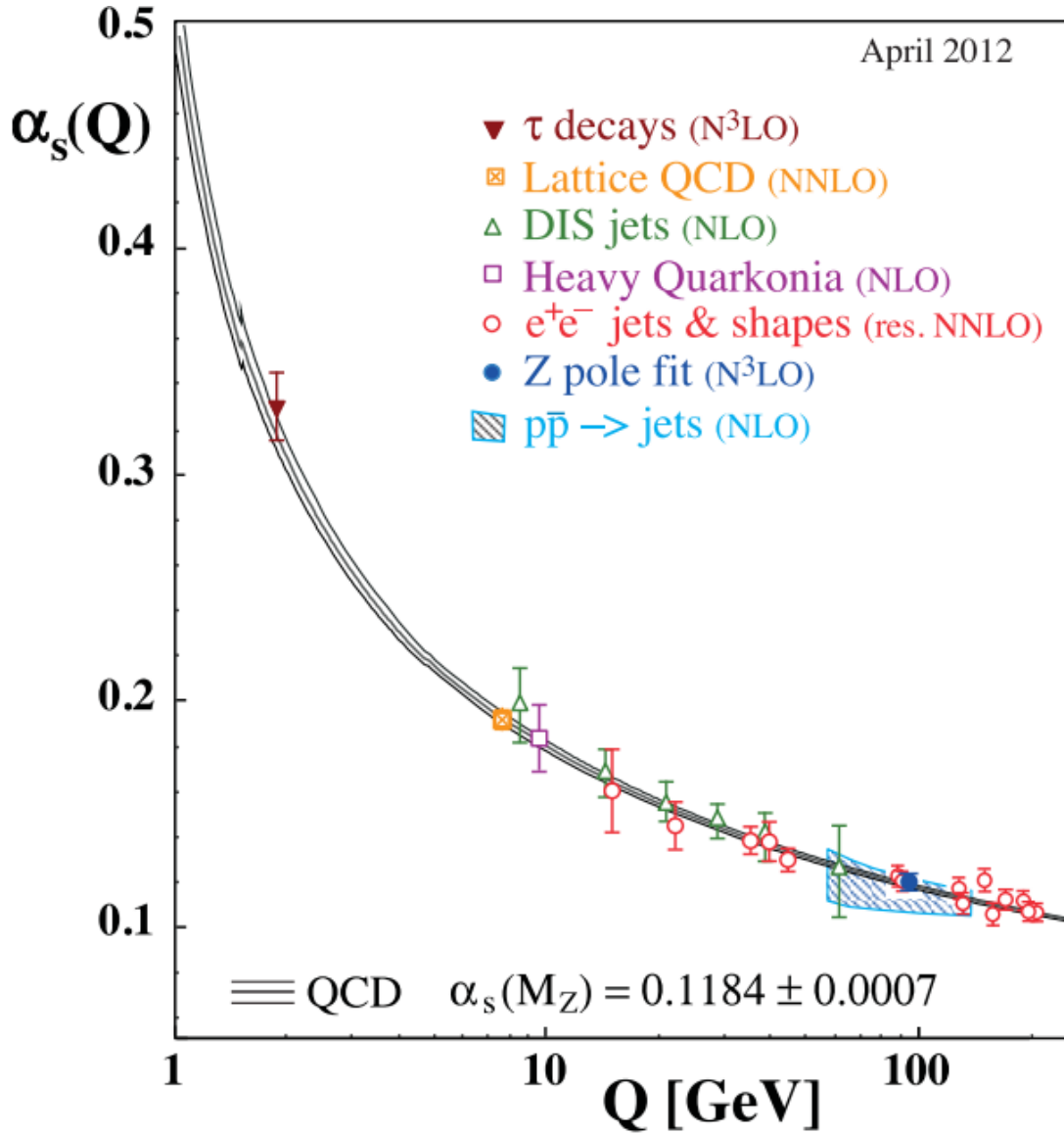


Figure 2.1: Summary of measurements of  $\alpha_s$  as a function of the respective energy scale,  $Q$ , from Ref. [17]. The respective degree of QCD perturbation theory used in the extraction of  $\alpha_s$  is indicated in brackets (NLO: next-to-leading order; NNLO: next-to-next-to leading order; res. NNLO: NNLO matched with resummed next-to-leading logs; N<sup>3</sup>LO: next-to-NNLO).

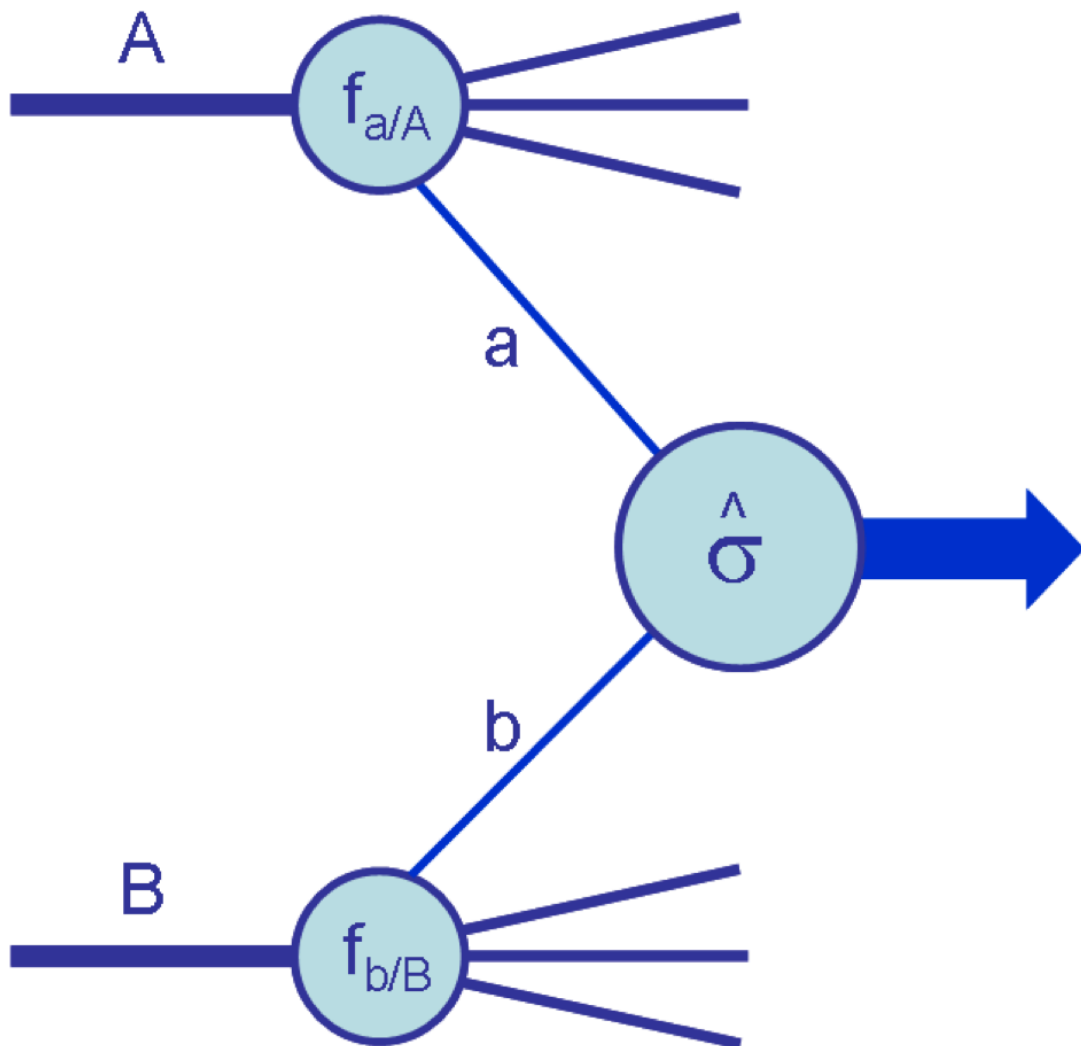


Figure 2.2: Diagram from Ref. [?] illustrating the structure of a generic hard scattering process of two incoming partons  $A$  and  $B$  with PDFs  $f_{a/A}$  and  $f_{b/B}$ .

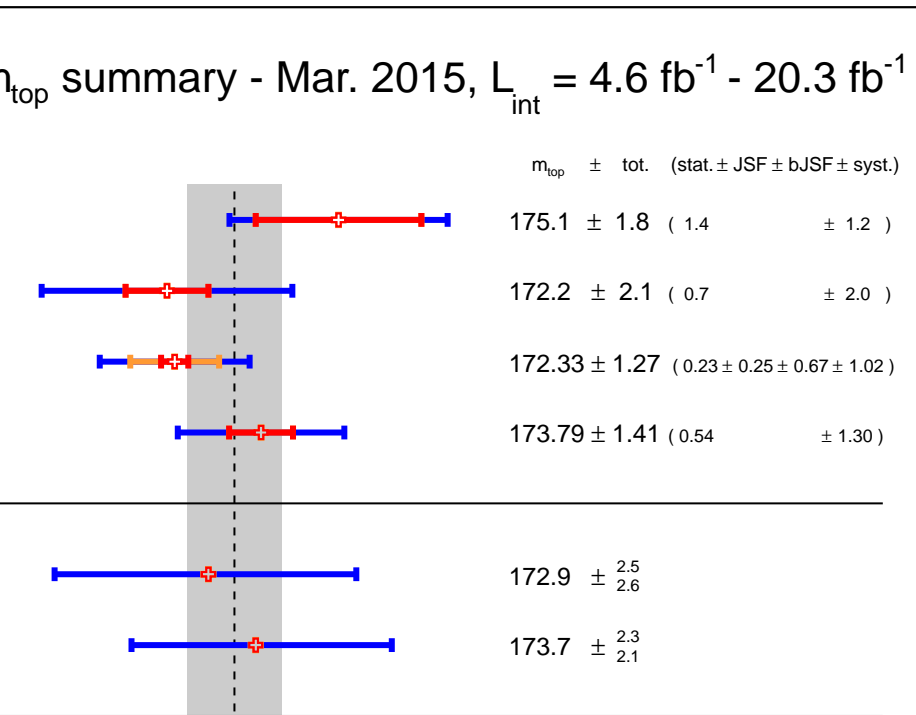


Figure 2.3: Summary of the ATLAS direct  $m_{top}$  measurements. The results are compared with the ATLAS, Tevatron and Tevatron+LHC  $m_{top}$  combinations. For each measurement, the statistical uncertainty, the sum of the remaining uncertainties are reported separately. The JSF, bJSF contains the JSF uncertainty in nature and apply to analyses performing in-situ (top quark pair) energy calibration procedures.

World Comb.  $\pm 1.6$

\*Preliminary,  $\rightarrow$  Input to ATLAS comb.

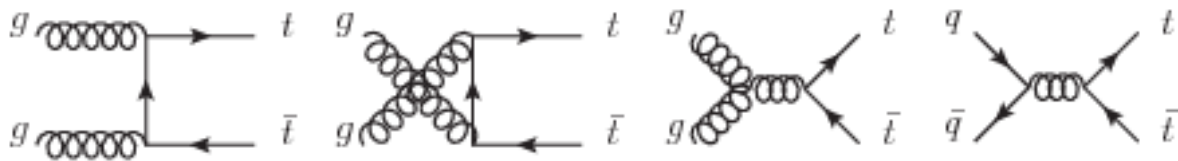


Figure 2.4: Feynman diagrams for  $t\bar{t}$  production at leading order QCD

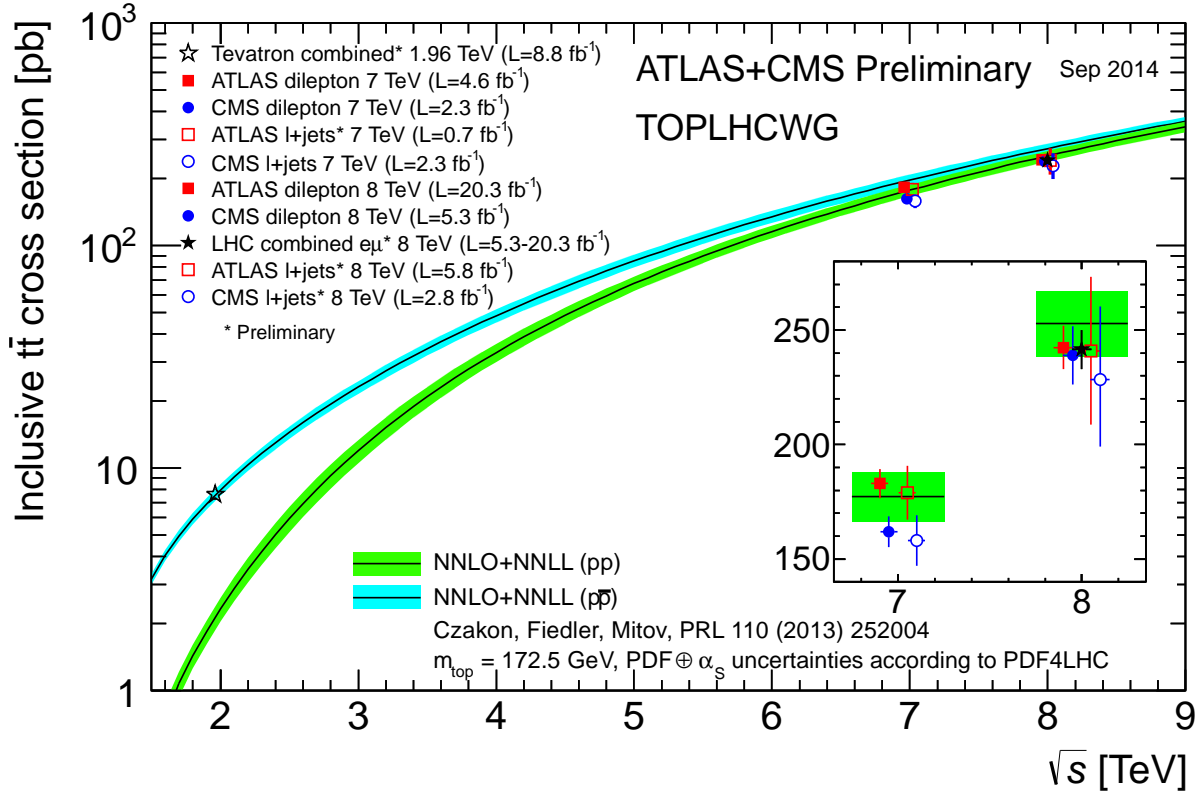


Figure 2.5: Summary of LHC and Tevatron measurements of the top-pair production cross-section as a function of the centre-of-mass energy compared to the NNLO QCD calculation complemented with NNLL resummation (top++2.0). The theory band represents uncertainties due to renormalisation and factorisation scale, parton density functions and the strong coupling. The measurements and the theory calculation is quoted at  $m_{\text{top}}=172.5 \text{ GeV}$ . Measurements made at the same centre-of-mass energy are slightly offset for clarity.



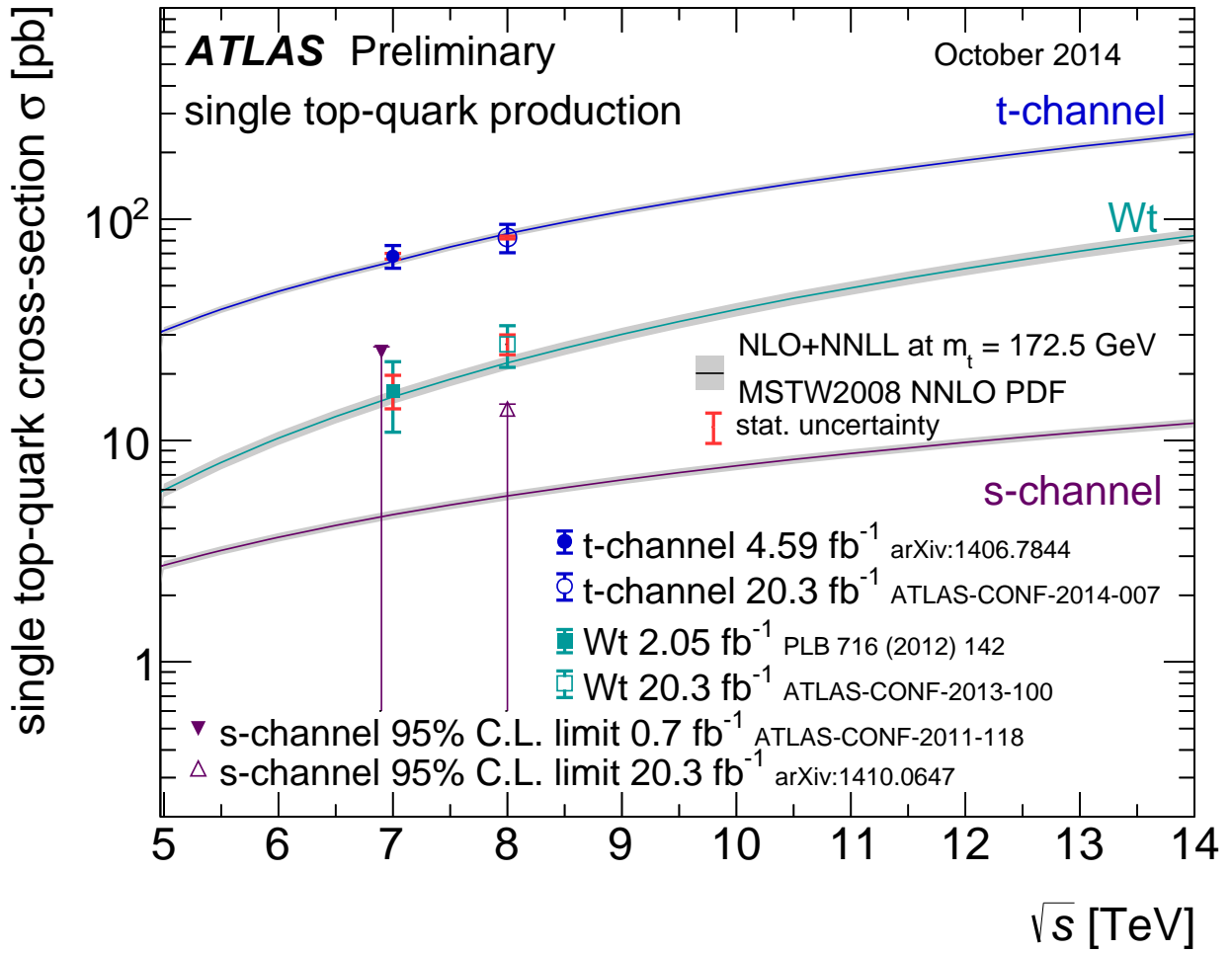


Figure 2.6: Summary of ATLAS measurements of the single top production cross-sections in various channels as a function of the center of mass energy compared to a theoretical calculation based on NLO QCD complemented with NNLL resummation. For the  $s$ -channel only an upper limit is shown.

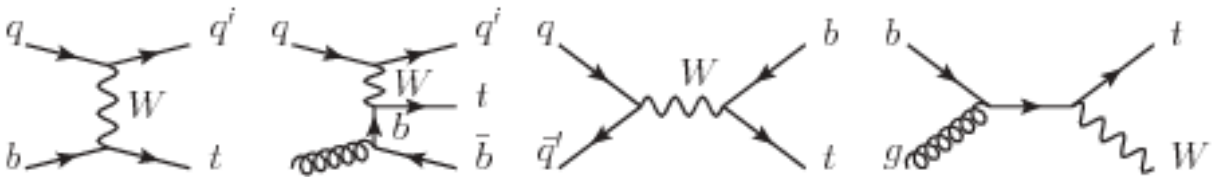


Figure 2.7: Feynman diagrams for single top quark production at leading order QCD. From left to right:  $t$ -channel production as flavor excitation;  $t$ -channel production as  $W$ -gluon fusion;  $s$ -channel production;  $Wt$ -channel production.

# Chapter 3

## Analysis strategy

3.1 Event selection

3.2 Extra jets

3.3 Correction procedure

3.4 Evaluation of generators

# Chapter 4

## The ATLAS detector and the LHC

### 4.1 The Large Hadron Collider

The Large Hadron Collider (LHC) ?? is the largest and most powerful particle collider that has ever been built. Construction of the LHC involved a collaboration of more than 10,000 scientist from more than 100 countries and was completed in 2008, after a decade of work. The cost of the machine alone is about 5 billion USD (3 billion Euro).

The European Organization for Nuclear Research (CERN) built the LHC in a tunnel underneath the border of France and Switzerland, near the city of Geneva. The LHC occupies a large tunnel 27 km in circumference that was originally constrected in the 1990s for the Large Electron Positron collider (LEP). Hadrons (either protons or ions) are accelerated and focused into two beams traveling in opposite directions around this tunnel. These beams are then made to collide with very high energy at one of the four collision points along the ring where their paths intersect. AEach of these points is home to one of the four main LHC experiments: A Large Ion Collider Experiment (ALICE) [1], ATLAS [2], the Compact Muon Solenoid (CMS) [3], and the Large Hadron Collider beauty (LHCb) experiment [4]. ALICE is a detector that looks at collisions of lead ions to study the properties of quark-gluon plasma. ATLAS is a general-purpose detector that looks for a wide range of possible new types of physics, including the Higgs boson, supersymmetry (SUSY) and extra dimensions. CMS is an additional general-purpose detector, designed and run independently from ATLAS, but with the same goals in mind. LHCb is a detector specially designed to study the asymmetry between matter and anti-matter in the interactions of B-particles. Figure 4.1 shows a aerial view diagram with the locations of these four experiments along the LHC ring. The location of the LHC ring in relation to the city of Geneva and the French-Swiss border is also illustrated.

The main goal of the LHC is to investigate unsolved questions in our current understanding of particle physics, such as the details of the Higgs mechanism, the existence of new particles from SUSY or extra dimensions and the source of dark matter and dark energy.

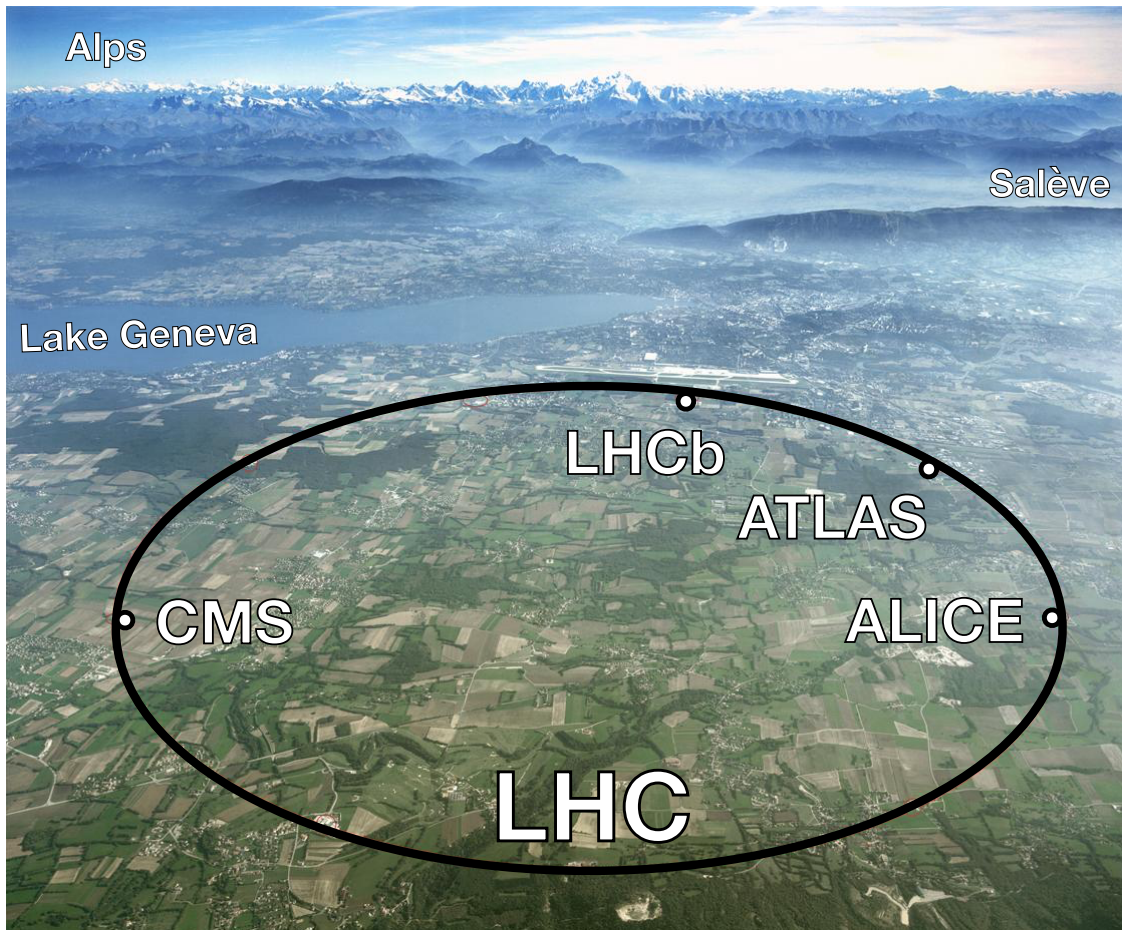


Figure 4.1: The location of the four main LHC experiments: ALICE, ATLAS, CMS and LHCb. The LHC tunnel is 27 km in circumference, situated underneath the border of France and Switzerland, near the city of Geneva, as shown. [6].

#### 4.1.1 Accelerator Complex

A succession of machines known as the “accelerator complex” accelerate particles to increasingly higher energies [13], shown in Figure 4.2. First, an electric field is used to strip protons from atoms in a simple bottle of hydrogen gas. Then, the first accelerator in the chain, Linac 2, accelerates protons to 50 MeV. Next, the beam is injected into the Proton Synchrotron Booster (PSB) and then the Proton Synchrotron (PS), which accelerate the protons to 1.4 GeV and 25 GeV respectively. After that, the Super Proton Synchrotron accelerates the protons to 450 GeV. The last step in the chain is the LHC; from the SPS, protons are transferred into the two beam pipes of the LHC and accelerated in opposite direction. Filling each of the rings of the LHC takes 4 minutes and 20 seconds, and it takes another 20 minutes to accelerate each beam to its final energy of 4 TeV. The same two beams will circle for many hours.

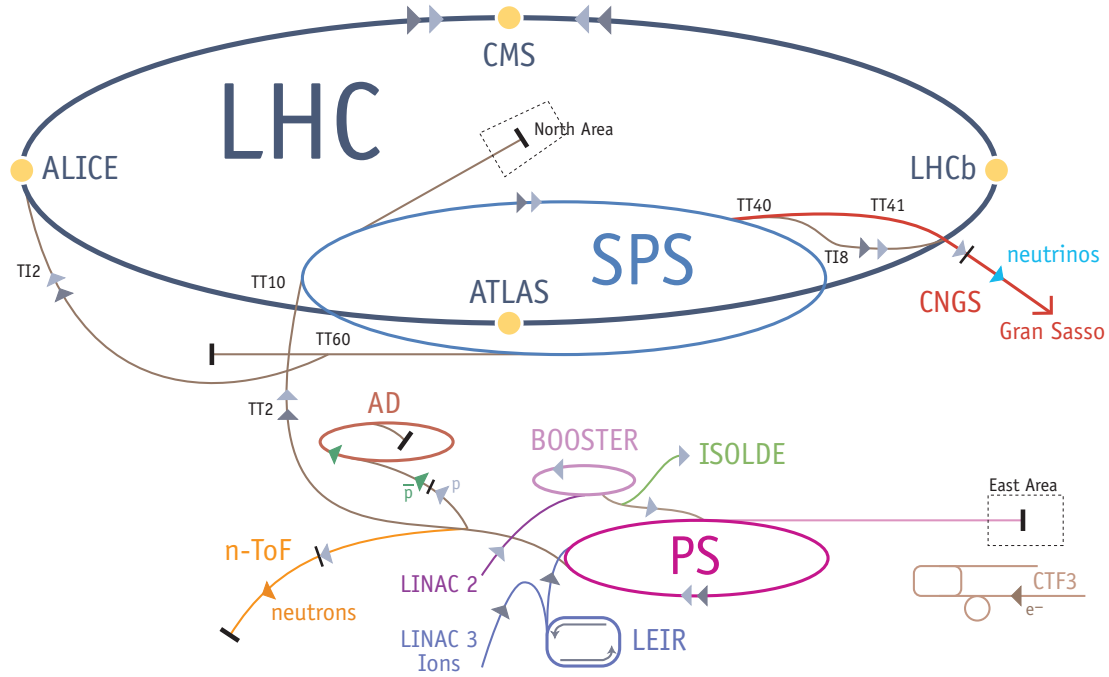


Figure 4.2: The LHC accelerator complex boosts particles to increasingly higher energies before reaching the LHC. The particle beams are accelerated successively by Linac 2, the Proton Synchrotron Booster (PSB), the Proton Synchrotron (PS), the Super Proton Synchrotron (SPS) and then finally enter the LHC rings [14].

Inside the LHC, the beams travel in opposite directions around separate rings called “beam pipes,” which are tubes kept at ultrahigh vacuum. The beams are directed by a collection of very strong superconducting electromagnets, including 1232 dipole magnets and 392 quadrupole magnets. Superconduction requires the magnets to be cooled to  $-271.3$  C. A distribution system of liquid helium keeps the magnets cool. The 15 meter long dipole magnets steer the beams around the ring, while the 5-7 meter long quadrupole magnets focus the beams before collision. The protons in the beams circulate in well-defined groups called *bunches*. Each bunch consists of approximately  $10^{11}$  particles, and each beam has 2808 bunches. This bunch structure maximizes the chances of collisions since multiple protons have the chance to collide each crossing. In 2012, bunch crossings occurred every 50 nanoseconds.

### 4.1.2 Beam conditions

Due to the Radio Frequency (RF) fields in the accelerating cavities, the proton beams are segmented into groups of protons called *bunches*. Each beam contains 2808 bunches, and each bunch contains  $1.7 \times 10^{11}$  protons. Many protons are included per bunch to maximize

the probability of a proton-proton collision for a given bunch crossing. A bunch crossing occurred every 50 nanoseconds during operations in 2012.

Given two equally bunched beams, the instantaneous *luminosity* ( $\mathcal{L}$ ) is given by:

$$\mathcal{L} = f \frac{n_1 n_2}{4\pi\sigma_x\sigma_y}, \quad (4.1)$$

where  $f = 11\,245.5$  Hz is the collision frequency of the LHC beams;  $n_1$  and  $n_2$  are the numbers of protons in each beam; and  $\sigma_x$  and  $\sigma_y$  are the RMS beam widths in the horizontal (bend) and vertical directions.[17] The maximum instantaneous luminosity of the LHC in 2012 was  $7.7 \times 10^{33}$

The instantaneous luminosity must be integrated over time because the beam conditions that go into Equation 4.1 are always changing over the duration of a run. The integral over time and varied beam conditions is called the integrated luminosity and can be used to relate the number of events  $N$  for a given physics process to its cross section  $\sigma$ :

$$N = \sigma \times \int \mathcal{L}(t)dt \quad (4.2)$$

In 2012, the total integrated luminosity of the LHC was  $20.3^{-1}\text{fb}$  with uncertainty of 2.8% [11]. The cumulative luminosity recorded over the course of 2012 is shown in Figure 4.3.

The beam conditions also determine the number of proton-proton interactions that occur in each bunch crossing. When a single bunch crossing produces multiple separate proton-proton collisions, these events are referred to as *pile-up*. Pile-up presents a significant challenge since it can rapidly increase the combinatoric complexity of reconstructing events and quickly degrades the performance of the reconstruction algorithms. In 2012, pile-up was much larger than anticipated. Figure 4.4 shows the mean number of interactions per bunch crossing for 2011 and 2012, demonstrating the substantial increase of pile-up events in the latter. Reconstruction challenges were overcome by optimizing the existing reconstruction algorithms, as well as new techniques for subtracting pile-up events from the physics of interest. Pile-up techniques used in this analysis will be discussed in the chapter on extra jet object selection.

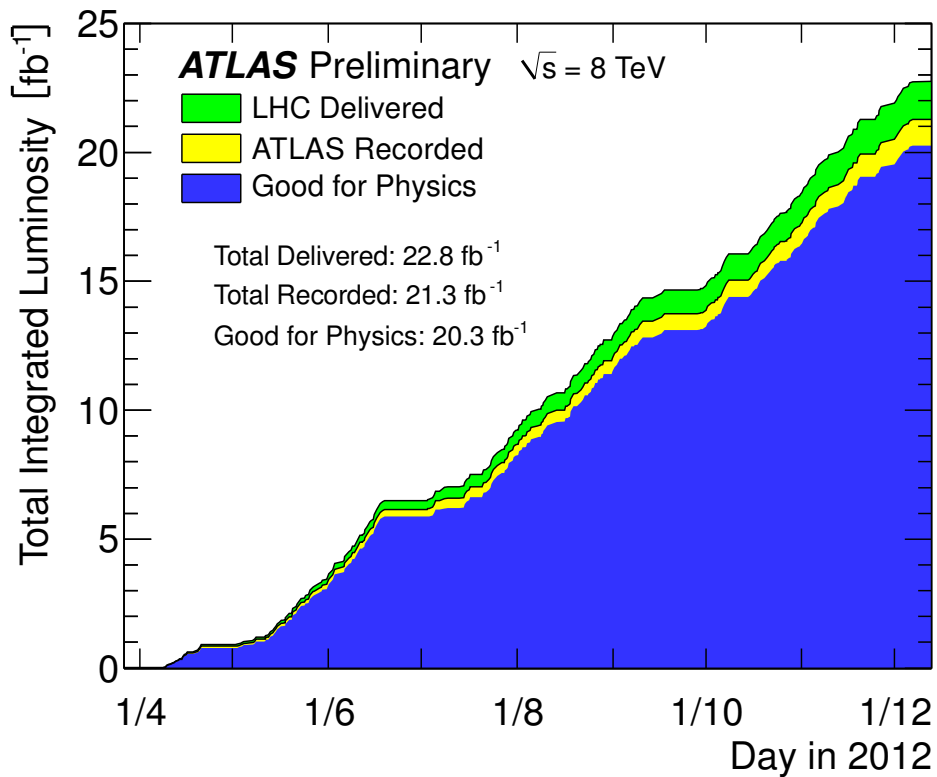


Figure 4.3: Cumulative luminosity versus time delivered to (green), recorded by ATLAS (yellow), and certified to be good quality data (blue) during stable beams and for pp collisions at 8 TeV centre-of-mass energy in 2012. Luminosity can be lost due to data acquisition inefficiency or other effects.

## 4.2 Overview of the ATLAS detector

### 4.3 Inner detector

#### 4.3.1 Pixel detector

#### 4.3.2 SemiConductor Tracker

#### 4.3.3 Transition Radiation Tracker

#### 4.3.4 Track reconstruction

### 4.4 Calorimeters

#### 4.4.1 Electromagnetic calorimeter

#### 4.4.2 Hadronic calorimeter

### 4.5 Muon spectrometer

### 4.6 The trigger system

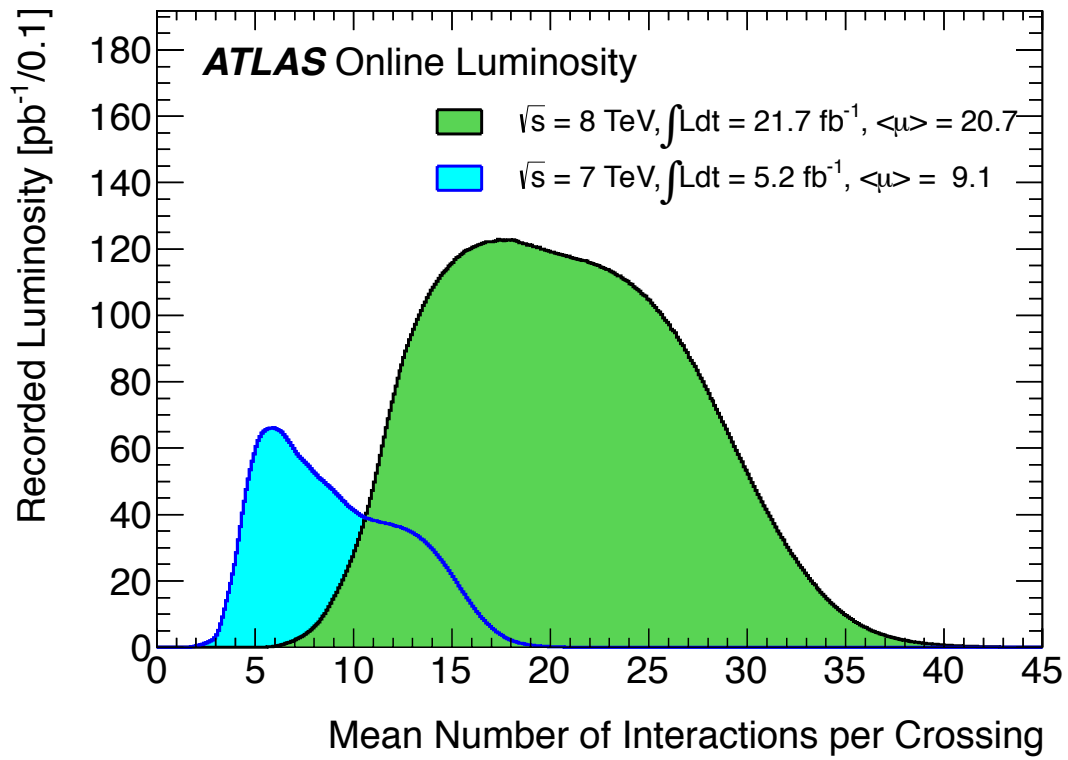


Figure 4.4: Luminosity-weight distribution of the mean number of interactions per bunch crossing. Both the full data from the 2011 and 2012  $pp$  runs at the LHC are shown.



# Chapter 5

## Event reconstruction and object definitions

### 5.1 Object reconstruction and selection

#### 5.1.1 Charged tracks

#### 5.1.2 Primary vertex

#### 5.1.3 Electron

#### 5.1.4 Muon

#### 5.1.5 Jets

#### 5.1.6 $b$ -jet identification

### 5.2 Particle-level definitions

# Chapter 6

## Event selection

### 6.1 Data samples

#### 6.1.1 Collision data

#### 6.1.2 Monte Carlo samples

##### 6.1.2.1 $t\bar{t}$

##### 6.1.2.2 Single top $Wt$

##### 6.1.2.3 Other physics processes

### 6.2 Event selection

#### 6.2.1 Event yields

#### 6.2.2 Reconstructed distributions

# Chapter 7

## Reconstruction of extra jets

7.1 Matching criteria

7.2 Background contributions

7.3 Reconstruction level distributions

# Chapter 8

## Correction to particle-level

### 8.1 Introduction to unfolding

### 8.2 Procedure

#### 8.2.1 Binning

#### 8.2.2 Bias in extra jets from event selection requirements

##### 8.2.2.1 Study of biases

##### 8.2.2.2 Correction factor

### 8.3 Validation

#### 8.3.1 Closure test

#### 8.3.2 Stress test

### 8.4 $\chi^2$ evaluation

# Chapter 9

## Sources of uncertainty

### 9.1 Types of uncertainty

Bias versus spread

### 9.2 Detector modeling

### 9.3 Single top rate

### 9.4 Background extra jets

### 9.5 Input extra jet spectrum

### 9.6 Combined uncertainty

# Chapter 10

## Results

10.1 Fully corrected distributions

10.2  $\chi^2$  comparisons

10.3 Discussion

## Chapter 11

## Conclusions

# Appendix A

## Extra jets

stuff



## Appendix B

### Tracking studies

## Appendix C

### Modeling hadron decays

# Bibliography

- [1] The alice experiment at the cern lhc. *Journal of Instrumentation*, 3:S08002, 2008.
- [2] The atlas experiment at the cern large hadron collider. *Journal of Instrumentation*, 3:S08003, 2008.
- [3] The cms experiment at the cern lhc. *Journal of Instrumentation*, 3:S08004, 2008.
- [4] The lhcb detector at the lhc. *Journal of Instrumentation*, 3:S08005, 2008.
- [5] A search for  $t\bar{t}$  resonances using lepton plus jets events in proton-proton collisions at  $\sqrt{s} = 8$  TeV with the ATLAS detector. Technical Report ATLAS-CONF-2015-009, CERN, Geneva, Mar 2015.
- [6] Atlas photos, 2015.
- [7] First combination of Tevatron and LHC measurements of the top-quark mass. 2014.
- [8] Georges Aad et al. Search for top squark pair production in final states with one isolated lepton, jets, and missing transverse momentum in  $\sqrt{s} = 8$  TeV  $pp$  collisions with the ATLAS detector. *JHEP*, 1411:118, 2014.
- [9] S. Abachi et al. Observation of the top quark. *Phys.Rev.Lett.*, 74:2632–2637, 1995.
- [10] F. Abe et al. Observation of top quark production in  $\bar{p}p$  collisions. *Phys.Rev.Lett.*, 74:2626–2631, 1995.
- [11] ATLAS Collaboration. Improved luminosity determination in  $pp$  collisions at  $\sqrt{s} = 7$  TeV using the ATLAS detector at the LHC. *Eur. Phys. J.*, C73:2518, 2013.
- [12] Micha Czakon, Paul Fiedler, and Alexander Mitov. Total Top-Quark Pair-Production Cross Section at Hadron Colliders Through  $O(\frac{4}{s})$ . *Phys.Rev.Lett.*, 110:252004, 2013.
- [13] Lyndon Evans and Philip Bryant. Lhc machine. *Journal of Instrumentation*, 3:S08001, 2008.
- [14] Christiane Lefevre. Lhc: The guide, 2009.

- [15] Ben Lillie, Lisa Randall, and Lian-Tao Wang. The Bulk RS KK-gluon at the LHC. *JHEP*, 0709:074, 2007.
- [16] Stephen P. Martin. A Supersymmetry primer. 1997. [Adv. Ser. Direct. High Energy Phys.18,1(1998)].
- [17] K.A. Olive et al. Review of particle physics. *Chin.Phys.*, C38:090001, 2014.
- [18] Michael Edward Peskin and Daniel V. Schroeder. *An introduction to quantum field theory*. Westview Press Reading (Mass.), Boulder (Colo.), 1995.